Boron in Ni-rich NCM811 cathode material: impact on atomic and microscale properties

Christoph Roitzheim[a,g], Liang-Yin Kuo[a], Yoo Jung Sohn[a], Martin Finsterbusch[a,b], Sören Möller[a], Doris Sebold[a], Helen Valencia[c,d], Maria Meledina[c,d], Joachim Mayer[c,d], Uwe Breuer[e], Payam Kaghazchi[a], Olivier Guillon[a,b,f], Dina Fattakhova-Rohlfing[a,g]*

[a]Institute of Energy and Climate Research – Materials Synthesis and Processing (IEK-1), Forschungszentrum Jülich GmbH, 52425 Jülich, Germany

[b]Jülich-Aachen Research Alliance: JARA-Energy, 52425, Jülich, Germany

[c]Central Facility for Electron Microscopy (GFE), RWTH Aachen University, 52074 Aachen, Germany

[d]Ernst Ruska-Centre (ER-C 2), Forschungszentrum Jülich GmbH, 52425 Jülich, Germany

[e]Central Institute for Engineering, Electronics and Analytics (ZEA-3), Forschungszentrum Jülich GmbH, 52425 Jülich, Germany

[f]Institute of Mineral Engineering, RWTH Aachen University, Mauerstr. 5, 52064 Aachen, Germany

[g]Faculty of Engineering and Center for Nanointegration Duisburg-Essen (CENIDE), Universität Duisburg-Essen, Lotharstraße 1, 47057 Duisburg, Germany

ABSTRACT: Doping of Ni-rich cathode active materials with boron is a promising way to improve their cycling stability and mitigate their degradation, but it is still not understood how this effect is achieved and where the boron is located. To receive deeper insights into the impact of doping on the atomic and microscale properties, B-doped $Li[Ni_{0.8}Co_{0.1}Mn_{0.1}]O_2$ (NCM811) cathode material was synthesized by a hydroxide co-precipitation as a model compound to verify the presence and location of boron in B-doped, Ni-rich NCM as well as its impact on the microstructure and electrochemical properties, by a combined experimental and theoretical approach. Besides X-ray diffraction and Rietveld refinement, DFT calculation was used to find the preferred site of boron absorption and its effect on the NCM lattice parameters. It is found that boron shows a trigonal planar and tetrahedral coordination to oxygen in the Ni-layers leading to a slight increase in lattice parameter c through an electrostatic interaction with Li ions. Therefore, B-doping of NCM811 affects the crystal structure and the cation disorder and leads to a change in the primary particle size and shape. To experimentally prove that the observations are caused by boron incorporated into the NCM lattice, we detected, quantified, and localized boron in 2 mol% B-doped NCM811 by ion beam analysis and TOF-SIMS. It was possible to quantify boron by NRA with a depth resolution of 2 µm. We found a boron enrichment on the agglomerate surface, but more importantly also a significant high and constant boron concentration in the interior of the primary particles near surface which experimentally verifies that boron is incorporated into the NCM811 lattice.

Keywords: Li-ion battery, Ni-rich cathode material, boron doping, ion beam analysis, DFT calculation

1. Introduction

Layered $Li[Ni_xCo_yMn_z]O_2$ (NCM) compounds are an extremely important class of cathode active materials (CAMs) for lithium-ion batteries (LIBs). Due to their high capacity, high operation potential and high rate capability they are the material of choice for high energy density LIBs, especially for the application in electrical vehicles (EVs). In the NCM class of compounds, Mn contributes to the structural stability at high cut-off potentials while Ni and Co have the greatest effect on the capacity. Particularly, the increase in the Ni content results in the increased specific capacity, however at the same time it deteriorates the structural and cycling stability because of the cation mixing, multiple phase transitions and mechanical failure during delithiation, and decreases the safety due to the enhanced possibility of thermal runaway.[1-5] Due to an unavoidable trade-off between the capacity and safety the attempts to improve both properties simultaneously in phase pure NCM materials are futile.[1] The efficient optimization strategies include therefore either doping of the host structure with multivalent cations[6], or formation of more complex morphologies with full or partial concentration gradients[7-11], surface coatings[6, 12-19] or core–shell structures[20-25]. Especially doping is well known to stabilize Ni-rich NCM based cathode materials during extended lithium extraction and insertion. The advantage of most dopants lies in higher M–O bond dissociation energies, which hinder oxygen release and mitigate the corresponding structural changes as well as the resulting volume change and microcrack formation during long-term cycling the battery. Additionally, the thermal stability of NCM in contact with liquid electrolyte is significantly enhanced by doping.[1, 5, 26] The penalty of doping is, however, the higher activation barriers for Li-ion mobility, which decrease the Li diffusion rate and the capacity due to the integration of electrochemically inactive elements.[5] Numerous dopants including Mg[27, 28],

$Al^{5, 28-32}$, Ti^{33}, Nb^{34} Cr^{32}, Y^{32}, Ga^{35}, $Fe^{5, 28}$, Sn^{5}, Zr^{36}, $B^{3, 37, 38}$, Mo^{39} and $W^{40, 41}$ have been already investigated.

From this wide variety, boron (B^{3+}) is a remarkably interesting doping element. Even with its small ionic radius of 0.27 Å, boron is able to block transition metal (TM) migration paths and to hinder the phase transition from layered to spinel structure during cycling of Ni-rich NCM.[42] S.-H. Han *et al.* were the first to report about the addition of B_2O_3 to $Li[Ni_{0.7}Co_{0.2}Mn_{0.1}]O_2$ (NCM721).[3] Especially at a high cut off voltage of 4.5 V, the boron containing sample showed significantly improved electrochemical performance due to a higher compressive stress and reduced crack formation during cycling. K.-J. Park *et al*. reported an improved capacity retention for 1 mol% B-doped highly Ni-rich $Li[Ni_{0.9}Co_{0.05}Mn_{0.05}]O_2$ (NCM90), which was also attributed to a reduced mechanical degradation during cycling.[37] Recently, C.-H. Jung *et al.* demonstrated that B-doped layered cathodes display better cycle stability not only by suppressed microcrack formation but also by its primary particles that have more lateral facets ((003) plane) which are stable against oxygen release.[43]

Although the beneficial impact of boron doping on the electrochemical performance of NCM is undeniable, it is still not understood how this effect is achieved and where the boron is located. Based on the results of X-ray diffraction, S.-H. Han *et al.* suggested that small-sized boron partially occupies the Li positions, while L. Pan *et al.* assumed a dual occupation of tetrahedral and octahedral interstitials (transition metal vacancies) by boron in the NCM structure.[3, 42] On the other hand, it is not even clear if boron is incorporated in the bulk structure of NCM or preferentially resides on its surface. Thus, K.-J. Park *et al*. have observed that boron doping changes the microstructure of the NCM90 particles. This effect was attributed to a decreased energy of the (003) surface in presence of boron, leading to the formation of microstructures with radially oriented primary particles that can relieve the strain induced by lithiation or delithiation during cycling. For the B-doped $LiNiO_2$ (LNO), DFT calculations have predicted the increase in the bulk lattice energy after the incorporation of boron atoms. As the most likely scenario for the structure stabilization, it was suggested that boron (together with neighbor O atoms) migrates into the topmost layer comprised of Li ions with the formation of an ordered lithium boron oxide structure (α-Li_3BO_3) on the particle surface.[37] However, an unambiguous experimental proof of any of these hypotheses is lacking and the exact position of boron in B-doped NCM morphologies is still unknown. In order to address this question, we systematically investigated the effect of B-doping on the crystal structure, microstructure, and electrochemical properties of $Li[Ni_{0.8}Co_{0.1}Mn_{0.1}]O_2$ (NCM811) with different boron concentrations using a combined experimental and theoretical approach. Our simulation determines the most favorable lattice position of boron dopant in NCM811 as well as changes in the lattice parameters with the doping level. Experimentally, we were able to detect and localize boron by ion beam analysis (NRA) and TOF-SIMS on the surface of secondary particles but also in the bulk of primary particles.

2. Experimental section

2.1. Synthesis

The cathode materials were synthesized by a modified hydroxide co-precipitation route reported before.[37, 44] The whole synthesis was performed under replenished argon atmosphere. Aqueous solutions of NaOH (Sigma-Aldrich, 98 %) (Solution 1) and NH_3 (aq) (Alfa Aesar, 28 %) (Solution 2) were prepared with appropriate concentrations. Additionally, a 2 M transition metal (TM) solution was prepared by dissolving $NiSO_4 \cdot 6H_2O$ (Alfa Aesar, 98 %), $CoSO_4 \cdot 7H_2O$ (Alfa Aesar, 98 %) and $MnSO_4 \cdot H_2O$ (Alfa Aesar, 99 %) with a molar ratio of 8:1:1, in deionized water.

The transition metal solution was dropwise added under vigorous stirring with an average flowrate of 45 ml/h into a 500 ml flask, containing an aqueous starting solution. Simultaneously, solution 2 (n(NH3 (aq))/n(TM) = 0.38) was added. The pH-value was precisely controlled by adding solution 1. After 5 h aging, the precipitated hydroxide was filtered and washed with deionized water. The remaining solid was dried at 80 °C in a vacuum oven (Memmert VO 500) for at least 14 h. After planetary ball milling (Fritsch Pulverisette 7) a fine light brown hydroxide precursor $(Ni_{0.8}Co_{0.1}Mn_{0.1})(OH)_2$ powder is obtained. In order to obtain the final NCM811, the hydroxide precursor was mixed with LiOH (Merck, 98 %) in a molar ratio of Li:(Ni + Co + Mn) = 1.03:1. In case of B-doped NCM811, the hydroxide precursor was in addition mixed with B_2O_3 (Sigma-Aldrich, 99.98 %) in a molar ratio of B:(Ni + Co + Mn) = x:1 (x = 0.013, 0.023, 0.033 and 0.043, depending on the desired boron concentration). The mixture was thoroughly ground in an agate mortar and calcined for 5 h at 480 °C and 10 h at 800 °C in an Al_2O_3 crucible under an oxygen containing atmosphere. A heating and cooling rate of 5 K min^{-1} was applied. After calcination, a fine grey powder is obtained.

2.2. Analytical techniques

The composition of the synthesized powders was analyzed by chemical analysis by inductively coupled plasma-optical emission spectrometry (ICP-OES, Thermo Scientific iCAP7600). The particle size distribution (PSD) was measured by a laser diffraction particle size distribution analyzer LA-950 (Horiba). Powders were dispersed in ethanol. The PSD was recorded before and after sonication. The presented values for D10, D50 and D90 were determined after sonication for 3 min. The evaluation is based on the Mie-theory by using a refractive index of 1.24.[45] The density of NCM powders was determined by using a gas pycnometer (Ultrapycnometer 1000, Quantachrome). BET-surface areas were determined by an AREA-mat (Jung Instruments GmbH).

Synthesized NCM powders were characterized for phase purity and crystal structure by using X-ray diffraction (XRD). X-ray powder diffraction was carried out using a D4 ENDEAVOR (Bruker AXS) with Cu-K_α radiation. For the qualitative phase analysis, powder XRD data were collected in a 2θ range of 10 – 80 °, with a step of 0.02 ° and a collecting time of 0.75 s/step. In case of Rietveld refinement, a 2θ range of 10 – 140 ° was chosen. The qualitative phase analysis of the diffraction patterns was carried out based on the powder diffraction file (PDF) database and the inorganic crystal structure database (ICSD) using the software HighScore (Malvern Panalytical).[46] Crystal structural refinement and determination of lattice parameters by means of Rietveld refinements were carried out with the software Topas V 4.2 (Bruker AXS).[47] Rietveld refinements for the samples NCM811_o and 2B-NCM811_o were performed using the program FullProf.[48] For morphology investigations, scanning electron microscope (SEM) images of pristine and B-doped NCM811 powders were taken by using the scanning electron microscope Zeiss Gemini 450. For powder analysis, the samples were prepared on a sticky carbon tape and coated with a thin platinum layer. For all samples secondary electron (SE) SEM images were shown. For higher and atomic resolution scanning transmission electron microscopy (STEM) was applied. An aberration corrected FEI Titan G2 80-200 STEM field emission electron microscope at 200 eV with Super-X EDS system[49] was used for high-angle annular dark field (HAADF) imaging and acquisition of energy-dispersive X-ray (EDS) elemental mapping. The powder samples were prepared by deposition on a Cu C-film grid and the cross-sections by using a focused ion beam (FIB) to extract a lamella out of the center of the particle.

Rutherford backscattering (RBS) and nuclear reaction analysis (NRA) were applied to characterize B-doped NCM811 powders which were fixed to carbon tape. The area analyzed by the ion beam was 200 μm in diameter. Therefore, only large agglomerates could be analyzed without the tape background. If these were not present, the carbon tape was accounted for by normalization to the metals present in NCM. The nuclear reaction $^{10}B(^{4}He, p_0)^{13}C$ was used for ^{10}B detection. The NRA measurement setup is described by S. Möller *et al.*[50]. For the detection efficiency calibration, a pure boron plate was analyzed, and the data evaluated considering the material specific stopping powers. The cross-sections from the work of H. Chen *et al.*[51] were used, since no better matching cross-sections were found in the literature. The comparison to the pure boron case showed a reasonable agreement with the thick target boron yields, in spite of the different reaction angles. The evaluation of the ion beam data was performed with the software SimNRA 7.02.[52] Time of flight secondary-ion mass spectrometry (TOF-SIMS) was applied for boron depth profiling using a TOFSIMS_5.NCS system (ION-TOF GmbH, Münster). Pristine and B-doped NCM powders were prepared by spreading them on an indium-foil and fixating them through self-adhesion. A 30 keV Bi^{+} primary beam for analysis and an 1 keV O_2^{+} beam for sputtering (to alter the analysis depth of the measurement) were scanned over an area of 400 μm by 400 μm, operating under non-interlaced mode (using a 1 s:1 s sputter:analyze cycle). The analyzed area by Bi beam was 130 μm by 130 μm, with either positive or negative secondary ions detected. Data analysis was carried out with SurfaceLab 7.0 (ION-TOF GmbH) software.

2.3. Electrochemical testing

For electrochemical activity tests electrodes with active material loadings of around 5 mg cm^{-2} were fabricated by casting a cathode slurry onto an Al foil. The slurries were prepared by mixing NCM, carbon black (Alfa Aesar, Super P® Conductive, 99+ % metal basis) and poly(vinylidene fluoride) (PVDF) (Alfa Aesar, mp: 155 – 160 °C) with a weight ratio of 90:5:5 in N-methyl-2-pyrolidone (NMP) (Alfa Aesar, 99+ %). For homogenization of the slurry, an ultrasonic bath and a planetary vacuum mixer (Thinky-mixer ARV-310) were used. A gap-bar coater (MTI, MSK-

AFA-HC100) with vacuum and heating function was utilized to cast the slurry on the Al foil. The resulting tape was afterwards dried for 30 min at 120 °C on the gap-bar coater and further dried in a vacuum furnace at 80 °C for 12 h. The cathode tapes were compressed using a conventional uniaxial press. For electrochemical investigations, cathodes with a diameter of 15 mm were punched. The electrochemical performance was evaluated in Coin cells (CR2032). The cells were assembled in an argon filled glovebox by using the NCM cathode, a glass fiber separator (Whatman) and a Li-metal foil (Alfa Aesar) as anode. As electrolyte served 1.0 M ($LiPF_6$) in ethylene carbonate (EC)/dimethyl carbonate (DMC)/ethylmethyl carbonate (EMC) (1:1:1 by volume) with 2 wt.% vinylene carbonate (VC) additive. Electrochemical tests were carried out at 25 °C by using a Bio-Logic VMP-300 multipotentiostat combined with a climate chamber (Vötsch Industrietechnik VT 4002EMC, Germany) whereas the data were evaluated by the software EC-lab. Cyclic voltammetry (CV) was performed in a potential range from 3.0 – 4.5 V vs. Li/Li^+ with a scan rate 0.05 mV s^{-1}. Galvanostatic cycling was carried out at different C-rates (0.04 C – 2 C; 1C = 160 mA g^{-1}) in a voltage window of 3.0 – 4.3 V vs. Li/Li^+. After the rate capability test long-term cycling was performed by constant current (cc) charge discharge at 0.5 C followed by constant voltage (cv) charge/discharge until a current of C/10 was reached. Electrochemical impedance spectroscopy (EIS) was performed at 4.3 V in a frequency range of 1 MHz to 10 mHz with an amplitude of 10 mV. For evaluation of the impedance spectra, the software ZView (Scribner) was used.

2.4. Theoretical approaches

Spin-polarized density functional theory (DFT) calculations were performed using the Projector Augmented-Wave (PAW)[53] pseudopotential method implemented in the Vienna Ab Initio Simulation Package (VASP) code.[54] The Perdew-Burke-Ernzerhof (PBE) functional[55] was employed to approximate the exchange-correlation (XC) energy for DFT calculations to find the most favorable structures. All the reported results in the simulation section are from DFT calculation using the strongly constrained and appropriately normed (SCAN) functional.[56] Total Coulomb-energy (E_C) calculations on various possible combinations were carried out using the *supercell* code.[57] The $Li[Ni_{0.8}Co_{0.1}Mn_{0.1}]O_2$ (NCM811) bulk was modelled using a 4×4×1 ($Li_{48}Ni_{40}Co_4Mn_4O_{96}$) supercell.[58] To determine the atomic positions for the Ni↔Li interchange cases, the following combinations were considered. For the case of 4 % Ni↔Li interchange, i.e. $(Li_{0.96}Ni_{0.04})(Li_{0.04}Ni_{0.76}Co_{0.1}Mn_{0.1})O_2$ modelled by $(Li_{46}Ni_2)(Li_2Ni_{38})Co_4Mn_4O_{96}$, all possible combinations of 2 Ni cations in 48 Li sites and 2 Li ions in 40 Ni sites, namely $\frac{48!}{2!46!} \times \frac{40!}{2!38!} = 1128 \times 780 = 8.8 \times 10^5$, were considered. For 2 mol% B-doping with a 4 % Ni/Li interchange, i.e. $(Li_{0.96}Ni_{0.04})(Li_{0.02}Ni_{0.76}Co_{0.1}Mn_{0.1}B_{0.02})O_2$, all possible combinations of 2 Ni cations in 48 Li sites, 1 Li ion in 40 Ni sites, and 1 B cation in 40 Ni sites, namely $\frac{48!}{2!46!} \times \frac{40!}{1!39!} \times \frac{39!}{1!38!} = 1128 \times 40 \times 39 = 1.8 \times 10^6$ configurations were modelled. DFT-PBE calculation was then performed on 5 structures with low E_C values for both cases, namely 4 % Ni↔Li interchange and 4 % Ni↔Li interchange + 2 mol% B→Li doping. By comparing total energy (E_{tot}) values of 5 structures with minimum E_c values for the B-doped case (with 4 % Ni↔Li interchange), we found a structure with 1 B cation (2 %) in the Ni/Mn-layer and 1 Li ion (2 %) in the Ni/Ni layer is the most favorable one. Therefore, we considered a similar structure for the interchange case in which boron was replaced by Li. The calculated E_{tot} value for this structure was found to be lower than those for structures with minimum E_c values. Thus, the lowest E_{tot} structure of 4 % Ni↔Li interchange was determined to be that with 1 Li ion (2 %) in the layer with only Ni cations (hereafter called the Ni/Ni layer) and 1 Li ion (2 %) in Ni and Mn ions (hereafter called the Ni/Mn layer). Afterwards, we checked another structure for the case of the B-doped case with 4 % Ni↔Li interchange in which 1 Li ion (2 %) was located in the Ni/Mn-layer, while 1 B cation (2 %) in the Ni/Ni-layer. It was found that this structure has a lower E_{tot} than that with 1 B cation (2 %) in the Ni/Mn-layer and 1 Li ion (2 %) in the Ni/Ni-layer. We modelled the atomic structure of the 8 % Ni↔Li interchange case from the 4 % Ni↔Li interchange one by considering two times more numbers of interchanges. To find the positions of 2 B cations in the supercell (4 mol% B-doping), i.e. $(Li_{0.92}Ni_{0.08})(Li_{0.04}Ni_{0.72}Co_{0.1}Mn_{0.1}B_{0.04})O_2$, the following replacements were considered for the structure with 8 % Ni↔Li interchange: 2B→2Li (in the Ni/Ni-layer), 2B→2Li (in the Ni/Mn-layer), and 1B→1Li (in the Ni/Ni-layer) together with 1B→1Li (in the Ni/Mn-layer). Finally, we found that the first structure has the lowest total energy among the considered structures. For all the E_c calculations, an average charge state of Ni, Co, and Mn is +2.96, and +2.92 for 2 mol% and 4 mol% B doping, respectively as well as a charge state of +3.00, +1.00, and −2.00 for B, Li, and O ions, respectively, were applied. DFT-PBE and SCAN calculations were carried out using a Gamma-centered 2×2×1 *k*-point mesh and an energy cut-off of 500 eV as well as an energy and force convergence criterion of 10^{-4} eV and 10^{-3} eV Å^{-1}.

3. Results and Discussion

Pristine $Li[Ni_{0.8}Co_{0.1}Mn_{0.1}]O_2$ (NCM811) as well as B-doped NCM811 materials with varying B content were synthesized via a hydroxide co-precipitation route. In a typical synthesis, the $Ni_{0.8}Co_{0.1}Mn_{0.1}(OH)_2$ precursor obtained in the first step was mixed with LiOH in a molar ratio of Li:(Ni + Co + Mn) = 1.03:1 and calcined at 800 °C under an oxygen containing atmosphere. The synthesis of B-doped NCM811 was performed in the same way with the difference that B_2O_3 was added in a molar ratio of B:(Ni + Co + Mn) = x:1 (x = 0.013, 0.023, 0.033 and 0.043 assigned further as 1B-NCM811, 2B-NCM811, 3B-NCM811 and 4B-NCM811, respectively) depending on the desired boron concentration. Chemical analysis (Table S1) confirms that the calcined materials have a targeted NCM composition and boron concentration. Powder XRD patterns correspond to phase pure materials with a hexagonal α-$NaFeO_2$ structure corresponding to the $R\bar{3}m$ (166) space group for pristine as well as B-doped NCM811 (**Figure 1**).[59] The clear peak splitting of (006)/(102) at 38 – 38.5 °(2θ) and (108)/(110) at 64 – 65 °(2θ) (**Figure 1**b,c) indicates the presence of an ordered hexagonal layered structure with high crystallinity.[60] No impurity phases were observed even for higher boron concentrations, no additional reflexes appear. In **Figure 1**c, there is an additional reflex beside (108) and (110) for NCM811 and 1B-NCM811 visible at 65° (2θ) which is device specific and caused by $k_{\alpha2}$ radiation. The sample 1B-NCM811 shows a slight peak shift towards higher angle due to the sample displacement while only the highly doped 4B-NCM811 shows a peak shift towards lower angle indication a lattice expansion only for this sample (**Figure 1**b,c). This is in agreement with the obtained lattice parameters which will be discussed below (**Table 1**). Based on the results of the XRD analysis of 4B-NCM811 it can be therefore concluded that boron trioxide was successfully incorporated into the lattice of NCM.

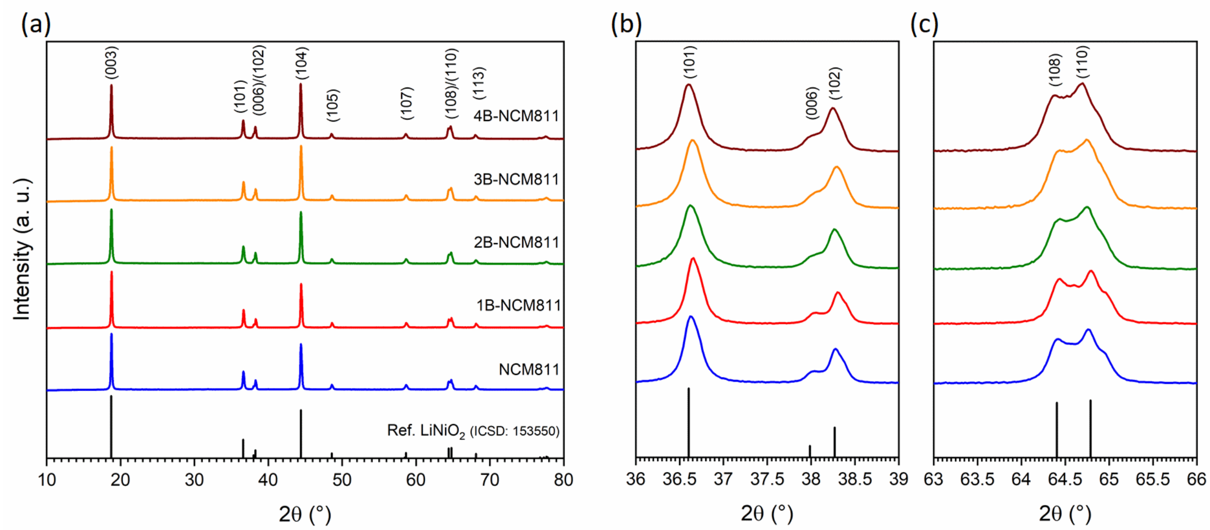

Figure 1. (a) Powder XRD patterns of pristine and B-doped NCM811 calcined at 800 °C. (b, c) Magnification of selected 2θ-regions from (a).

The possible effect of B-doping on the particle size and morphology was investigated. The particle size distribution (PSD) of NCM811 is unaffected by B-doping for our synthesis approach. The powders consist of hard agglomerates (secondary particles) with a D50 of 15.0 µm and 14.2 µm for pristine NCM811 and 2B-NCM811, respectively. The PSDs are shown in the supporting information (Figure S1). A further increasing of the boron concentration does not influence the particle size distribution as displayed in Table S2.

SEM analysis indicates that all synthesized powders are composed of spherical agglomerates (**Figure 2**a). Higher magnifications (**Figure 2**b–f) of these secondary particles indicate that each individual agglomerate is composed of nano-sized cuboidal primary particles. From **Figure 2**, it is obvious that the shape of those primary particles changes slightly from cuboidal to plate-like for higher boron concentrations. The 2B-NCM811 and 4B-NCM811 primary particles are thinner and more densely packed which results in a denser and smoother surface of the agglomerates (**Figure 2**d,f). In contrast to calcined NCM811, the NCM811 hydroxide precursor (Figure S2) consists of thin plate-like primary particles which indicates that during calcination a densification and particle growth towards cuboidal shape is taking place, especially for pristine NCM811. The doping has a strong effect on the average primary particle size, which progressively decreases with an increase in boron content. The primary particle size is around 200 nm for the pristine and 1B-NCM811 whereas it decreases to only 147 nm for the 4B-NCM811. In presence of boron (especially for 4 mol%) the particle growth during calcination appears to be inhibited resulting in smaller and thinner primary particles as reported by C.-H. Jung *et al*.[43]. A similar reduction of primary particle size due to B-doping was also reported by K.-J. Park *et al*.[37] for B-doped highly Ni-rich NCM90. While the primary particle size decreases, the specific BET surface area reduces dramatically from 1.56 $m^2 g^{-1}$ to 0.69 $m^2 g^{-1}$ and further to 0.32 $m^2 g^{-1}$ for pristine, 2B-NCM811 and 4B-NCM811, respectively, indicating an overall densification of the agglomerates surface. This result agrees with the work of L. Pan *et al*.[42] who also reported a strongly reduced specific surface area by B-doping of cathode materials. The density of our NCM811 powders was slightly increased by 2 mol% B-doping.

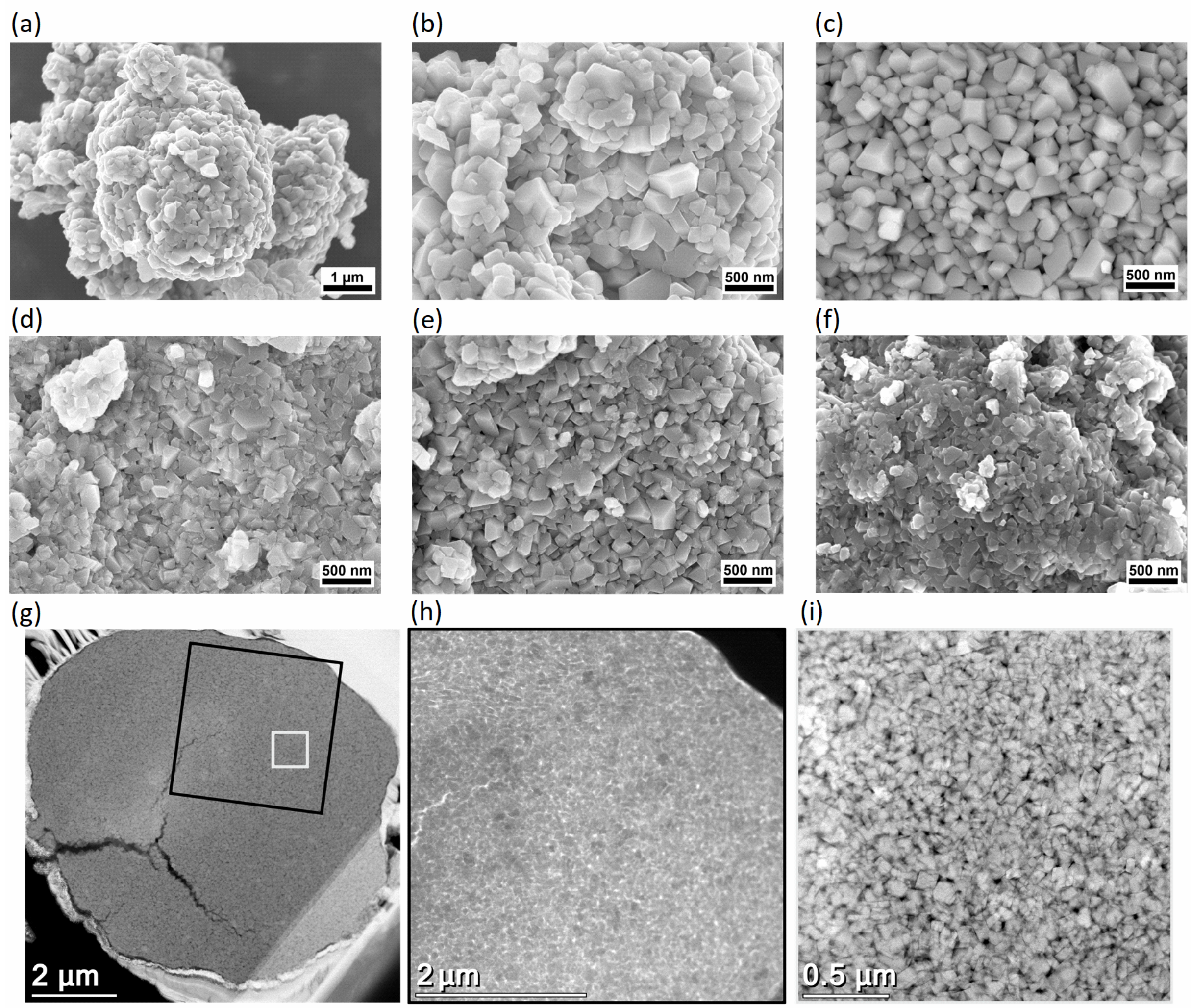

Figure 2. SEM secondary electron (SE) images (8 kV) visualizing (a) a typical secondary particle of pristine NCM811 as well as higher magnifications of primary particles of (b) pristine NCM811, (c) 1B-NCM811, (d) 2B-NCM811, (e) 3B-NCM811 and (f) 4B-NCM811. In (g-i) cross-sectional HAADF-STEM images of an agglomerate of 2B-NCM811 with different magnifications are shown. (h) and (i) show magnifications of the cross-sectional surface marked with black and white square in (g), respectively.

High-angle annular dark filed scanning transmission electron microscopy (HAADF-STEM) images and energy-dispersive X-ray (EDS) element analysis of 2B-NCM811 reveal a homogenous distribution of Ni, Co, Mn and O within the primary particle (Figure S3). No significant signal of boron was seen which could be related to a low concentration of boron of only 2 mol%, its homogeneous distribution within the grains and the detection limit of EDS analysis.

A cross-sectional HAADF-STEM image of a 2B-NCM811 prepared by focused ion beam (FIB) (**Figure 2**g-i) clearly demonstrates that the secondary particles are composed of randomly oriented primary particles. This morphology is different from the one reported by K.-J. Park *et al.*[37] for the highly Ni enriched $Li[Ni_{0.9}Co_{0.05}Mn_{0.05}]O_2$ (NCM90) doped with 1 mol% B. Namely, K.-J. Park *et al.* have demonstrated that the non-doped NCM90 agglomerates consist of randomly oriented short and thick primary particles, while B-doping results in a very different secondary particles morphology composed of the radially grown elongated primary particles. The change in the microstructure was attributed by the authors to a surface energy modification by B-doping.[37] In contrast to this publication, we did not observe similar microstructure for our 2B-NCM811 under the applied synthesis conditions, which leads to the conclusion that the microstructure optimization is not the only effect of the B-doping. In fact, an ammonia concentration gradient during the precursor co-precipitation can also lead to radially arranged primary particles.[61] Additionally, the oxygen partial pressure during the calcination step further influences the growing direction of the primary particles.[62] Thus, we assume that the B-doping leads to a preferred growing direction only in combination with a precise adjustment of the synthesis conditions or only for highly Ni-enriched cathode materials.

The absence of a secondary phase in the XRD patterns and the modified microstructure of B-doped NCM811 indicate a successful B-doping of the NCM lattice. The lattice parameters for pristine NCM calculated from the XRD patterns using the Rietveld refinement (**Table 1**, Figure S4) fall within the span reported in literature. It should be noted that the literature values scatter a lot due to the variation in Li and transition metal (TM) concentration as well as cation disorder (a = 2.8661 – 2.8805 Å; c = 14.2021 – 14.249 Å; c/a = 4.937 – 4.972).[63-66] For the B-doped NCM811, the obtained lattice parameters do not dramatically change when considering the measurement uncertainties, indicating a high structural similarity to the pristine sample. Only for 4B-NCM811 a slightly increased a parameter was found. Our findings differ from the observations of other groups for Li-rich and highly Ni-rich NCM, for which expansion of lattice parameter and unit cell due to B-doping was reported.[37, 38, 42]

Table 1. Summary of lattice parameters and Rietveld refinement results of pristine and B-doped NCM. Ni_{Li} gives the fraction of Ni ions occupying Li sites.

Active material	*a* [Å]	*c* [Å]	V [Å^3]	c/a	I(003)/I(104)	Ni_{Li} [%]
NCM811	2.878(1)	14.206(6)	101.90	4.94	1.09	7.5
1B-NCM811	2.877(1)	14.206(6)	101.83	4.94	1.07	7.5
2B-NCM811	2.878(1)	14.202(9)	101.87	4.93	1.01	6.3
3B-NCM811	2.879(1)	14.207(9)	101.98	4.93	1.00	8.8
4B-NCM811	2.881(1)	14.215(9)	102.18	4.93	1.00	10.0

The c/a ratio can be used as an indicator for the degree of cation disorder/cation mixing (interchange between Li and Ni sites), which is a critical factor for Ni-rich NCM. For an ideal hexagonal closed packed lattice with $R\bar{3}m$ (166) and layered structure, c/a = 4.99. Partial cation mixing is indicated by c/a < 4.96. If c/a = 4.90, a phase transition took place, an ideal cubic close packed lattice ($Fm\bar{3}m$ (255), rock-salt structure) is present and the peak splitting of the (006)/(102) and (108)/(110) Bragg reflections completely disappears.[67, 68] For our pristine NCM811 the c/a ratio is smaller than 4.96 indicating a severe cation disorder in our reference material. The degree of disorder can be estimated from the work of S. Gao *et al*.[66] who reports 11.37 % Ni on Li sites for the c/a = 4.937. For our B-doped NCM811 the c/a ratio slightly decreases, indicating that the introduction of boron results in a further increase in the cation disorder. An increasing Ni amount on Li sites is additionally verified by the reflex intensity ratio I(003)/I(104) (**Figure 1**a, **Table 1**) which continuously decreases by increasing the boron doping level in NCM811. The expansion of lattice parameter *a* and the changes in cation disorder for the B-doped NCM811 are further indications for the incorporation of boron into the NCM lattice.

L. Pan *et al*.[42] proposed a possible lattice site occupation of the incorporated boron. In trace amounts B^{3+} mainly occupies the tetrahedral interstitial of the packed oxygen in the transition metal (TM) and lithium layer, which enlarges lattice parameters *a* and *c* notably. When the concentration of boron increases it mainly occupies the transition metal vacancies in addition to the tetrahedral interstices like for low boron amounts. Thus, the cell parameters of the high-doped samples show no obvious increase as compared to the low doped one, since the volume of the octahedral interstice in the TM layer is significantly larger than that of B^{3+}. To confirm this hypothesis for our materials, Rietveld refinement was exemplary performed for 4B-NCM811, placing boron in the tetrahedral interstitials (Figure S4 and Table S3). No reasonable results could be obtained when boron was placed on the 6*c*-Wyckoff position. Much better fitting however was obtained for the boron on the TM positions (3*b*-Wyckoff position), in a good agreement with the results of L. Pan *et al.* who chose the same position for high and low B occupancy.[42]

Based on the Rietveld refinement, different degrees of cation disorder were found in dependence of the doping level for our material (**Table 1**) – the interchange fraction increases by B-doping, especially for 4B-NCM811 with 10.0 % Ni on Li sites. 2B-NCM811 shows the smallest Li–Ni interchange; however, for pristine NCM811 and lower doping concentrations the level of cation disorder is very similar. The determined percentages of Ni on Li sites based on Rietveld refinement show the same trend of an enhanced cation disorder by B-doping, as found by studying the c/a and the I(003)/I(104) ratios. Slight deviations from the observed trend of cation disorder have been observed especially for the 1B-NCM811 and 2B-NCM811 samples, which can however result from the accuracy of refinement and the made assumptions.

In general, the similar ionic radii of Li^{+} (0.72 Å) and Ni^{2+} (0.69 Å) allow the migration of Ni^{2+} to the Li layer.[41] It is well known that the valence state of the TM ions in NCM is not fixed. It is usually a combination of Ni^{2+}/Ni^{3+}, Co^{3+}/Co^{4+} and Mn^{3+}/Mn^{4+} [66], which explains the possibility of cation disorder in pristine NCM. If B^{3+} is introduced, a reduction of the valence state of the TM ions is assumed to obtain charge neutrality. If Ni^{3+} (0.56 Å) is reduced to maintain the charge balance, the abundant Ni^{2+} increases the probability for cation disorder.[41]

Atomic resolution Z-contrast HAADF-STEM imaging was performed for pristine and 2B-NCM811 to address and visualize cation disorder as well as possible structural changes induced by B-doping on the atomic scale. HAADF-STEM images for pristine NCM811 (**Figure 3**a) show a surface region (green squares) with a clear structural defect and an inner region (blue square) with a well order layered structure. An overlap with the schematic structure of NCM811 (**Figure** 3a, purple square) shows that in the surface region (2 – 3 nm in thickness) atomic contrast in the Li columns was obtained, while Li is too light to be imaged in HAADF-STEM mode. The contrast on the Li positions might result from transition metal ions (most probably, Ni^{2+}) occupying the Li sites. These results come in a good agreement with the cation disorder for pristine NCM811 proposed on the base of XRD analysis. STEM analysis reveals that the cation disorder is mainly found in the surface region. Fourier transforms (FFTs) of the surface region (green squares) and the interior region (blue square) display that the desired layered structure ($R\bar{3}m$) is present in the inner region while the surface region shows a rock-salt structure ($Fm\bar{3}m$). Based on XRD investigations an enhanced degree of cation disorder was found for 2B-NCM811 and therefore changes atomic structure could be assumed. The HAADF-STEM image of a 2B-NCM811 primary particle is depicted in **Figure 3**b.

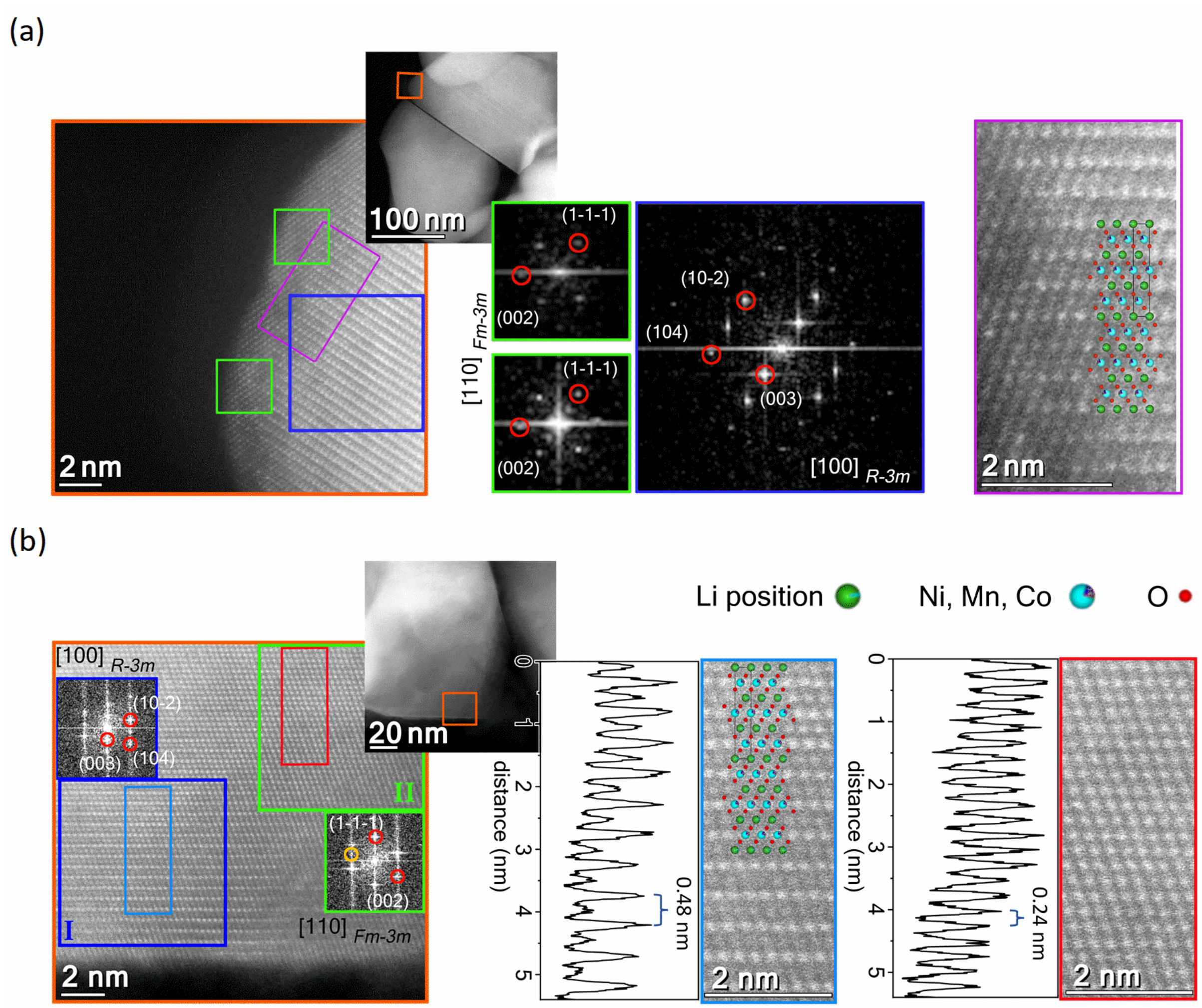

Figure 3. STEM analysis of pristine and 2B-NCM811 primary particles on the surface of agglomerates. (a) Overview and high resolution (HR) HAADF-STEM images of pristine NCM811 together with FFTs from the labelled areas. (b) Overview and HR HAADF-STEM images of 2B-NCM811 together with FFTs and the contrast line scans from the labelled areas.

Similar to the pristine NCM811, two regions with a different structure (region-I, blue square and region-II, green square) were identified also for the B-doped NCM (**Figure 3**b). The FFT of region-I (surface) reveal the desired layered structure ($R\overline{3}m$). In region-II a rock-salt structure ($Fm\overline{3}m$) has formed, where some remnant spots similar to the FFT of region-I are marked with a yellow circle. In **Figure 3**b a line scan showing the intensity distribution along the [100] ($R\overline{3}m$) direction on the surface region-I (light blue rectangle) shows an alternating atomic contrast with a periodicity of 0.48 nm caused by transition metal (TM) atoms. Atomic contrast with significantly lower intensity is visible in the rows where the Li sites are expected. This could be due to TM ions (most probably, Ni^{2+}) partially occupying the Li site (cation disorder). For 2B-NCM811, the cation disorder found in the surface region is less severe than that reported for the pristine NCM811. For the interior region-II (red rectangle) shown on the right of **Figure 3**b, the contrast line scan along the [110] ($Fm\overline{3}m$) direction indicates a periodicity of 0.24 nm which indicates that in region-II intense atomic contrast is present on all Li positions. Most possible reason for this observation is (i) severe cation disorder – when the amount of the TM in their initial sites is similar to the amount of TM in Li sites. However, this effect could also be caused by (ii) defects in the underneath lying atomic layers shift the TM atom column to the position of Li or (iii) thickness contrast: if the particle is thicker at the center than on the surface. For pristine NCM811, a well ordered hexagonal layered structure was found in the bulk of the primary particle while a surface layer with strong cation disorder and rock-salt structure was visible. In contrast to pristine NCM811, the B-doped NCM811 does not show a rock-salt structure on the surface region. By B-doping an ordered surface region with only a weak cation disorder and layered structure was found.

Based on our X-ray diffraction and Rietveld refinement, it is indicative that small sized boron occupies the larger TM positions which is confirmed by the similar lattice parameters for B-doped

NCM. However, the lattice position of boron in B-doped NCM and the reason for the nearly constant lattice parameters are still unclear since other factors like cation disorder as well as changes of the electronic environment in the NCM lattice cannot be excluded. Therefore, DFT calculation was used to study the location of boron atoms and their influence on the NCM811 lattice. Since the experimental analysis of the powders by XRD showed a Ni↔Li interchange in the absence of B-doping, we first considered the influence of cation interchange on the lattice parameters for pristine NCM811. It was found that the Ni↔Li interchange without B-doping causes the lattice parameters *a* and *c* to shrink (**Figure 4**a). This is due to the strengthening of electrostatic attraction between Li- and O-layers with Ni^{2+}↔Li^{+} interchanges by which the O–TM–O interlayer separation, namely d_z(O–Li–O) (average O–Li–O distance), reduces from 2.588 Å to 2.555 Å. The average O–TM–O intralayer distance d_z(O–TM–O) only slightly expands from 2.112 Å to 2.121 Å.

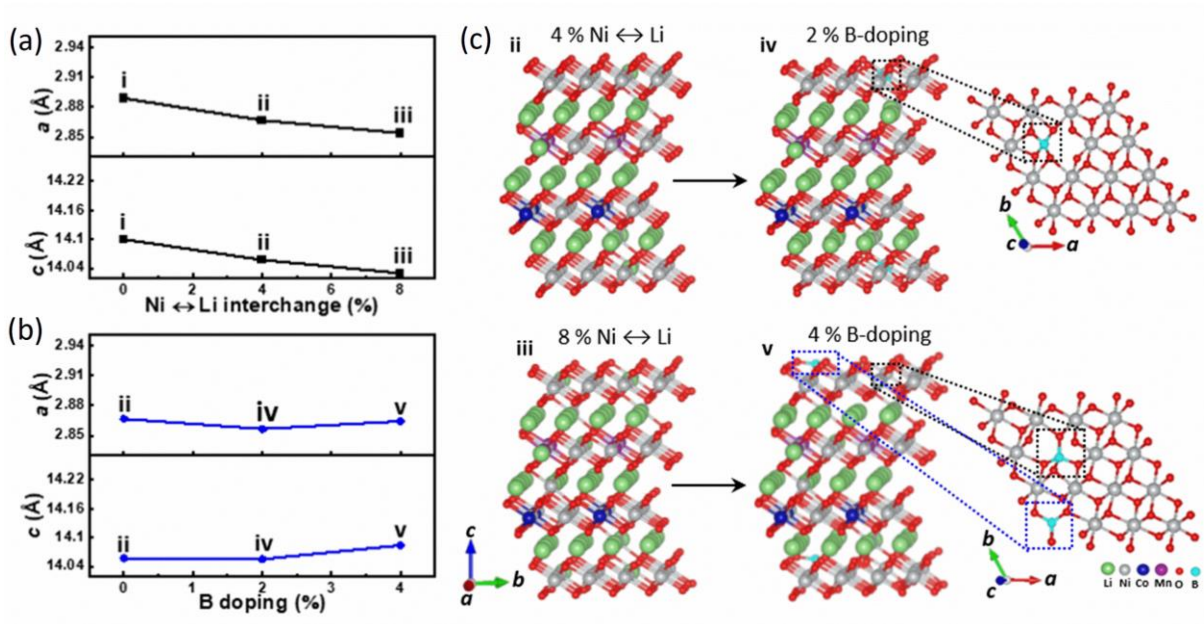

Figure 4. Calculated changes in lattice parameters *a* and *c* in NCM811 with (a) Ni↔Li interchange and (b) B-doping. (c) Atomic structures of NCM811 before and after B-doping as well as coordination of boron to oxygen.

Doping with a large amount of boron alleviates the lattice size change induced by the Ni^{2+}↔Li^{+} interchange (**Figure 4**b). Thus, in agreement with experimental data, we found that when boron is incorporated in the structure and the Ni^{2+}↔Li^{+} interchange is enhanced, no significant impact on the *a* and *c* values is observed. This is in strong contrast to the non-doped system, for which even the slight increase in the degree of Ni↔Li interchange (from 0 % to 4 %) results in a linear decrease in *a* and *c* values. To better understand the effect of B-doping we focus on the 2 mol% and 4 mol% B-doped structures with the magnified doping effects. Our calculations indicate that *a* remains almost unchanged, while *c* slightly expands with 4 mol% B. The increase in *c* in this case is due to the B-induced expansion of both d_z(O–Li–O) (2.56 Å → 2.57 Å) and d_z(O–TM–O) (2.12 Å → 2.13 Å). The former change is because of a stronger repulsion between B and Li compared to Ni and Li. This is due to the fact that the B–Li distances ($d_{B–Li}$: 2.31 Å – 2.60 Å) are shorter than the Ni–Li ones ($d_{Ni–Li}$:2.70 Å – 3.04 Å). The slight expansion of d_z(O–TM–O) is because of an up-ward displacement of O anions that bind to B to accommodate this cation. The simulation shows that 2 B cations in the supercell (4 mol% B-doping) occupy a trigonal planar and an almost tetrahedral site in the O–Ni–O layer (**Figure 4**c, structure v). The B cation in the case of 2 mol% B-doping occupies a tetrahedral site (**Figure 4**c, structure iv). Reported values of $d_{B–O}$ for the trigonal planar sites in the most stable phase of boron oxide, namely B_2O_3 (P31), are ≈ 1.34 Å – 1.40 Å.[69] However, the experimental study by R. Shannon *et al.*[70] on a high-pressure form of B_2O_3 (Ccm21) has found $d_{B–O}$ of 1.51 Å for three B-O bonds and 1.37 Å for one B–O bond. The calculated values of $d_{B–O}$ in the structure v are 1.37 Å – 1.59 Å. Note that due to the shorter bond length of B–O compared to that of Ni–O, occupation of octahedral sites is not possible for boron. Calculated values of $d_{Ni–O}$ in the Ni-layer of the structure v lie between 1.85 Å and 2.27 Å. **Figure 4** shows that the *c* value does not change much with 2 mol% B-doping. The reason behind this behavior is that B occupies a tetrahedral site so that it stays almost in the Ni-layer plane. As such, the values of $d_{B–Li}$ for nearest neighbors are 2.65 Å and 2.88 Å, which are longer than those for the 4 mol% B-doping case ($d_{B–Li}$: 2.31 Å – 2.60 Å) and more comparable to $d_{Ni–Li}$ values of 2.70 Å – 3.04 Å. **Figure 4**a,b shows a clear increase in the *a* value of structure iii when it is doped by 4 mol% boron (structure v). This is most likely due to the migration of one of B cations from the Ni-layer plane to the O-layer plane (to form the B–O trigonal) leaving a TM vacancy and weakening of planar TM–TM repulsion. A similar reason can be applied to explain the small increase in *a* when a larger amount of boron is incorporated (structure iv → structure v). The theoretical approach provides an insight into the lattice position of boron atoms in B-doped NCM811. As shown by the atomic structures iv and v (**Figure 4**c) for 2B-NCM811 and 4B-NCM811, respectively, the coordination of boron to oxygen depends on the doping level. Boron occupies tetrahedral sites for 2 mol%, while trigonal planar as well as tetrahedral sites were occupied for 4 mol% doping. The different coordinations have an impact on the change in lattice parameter *c*. Furthermore, the simulated lattice parameters considering both effects, namely B-doping and B-induced increase in the Ni↔Li interchange (**Figure 4**b), show only minor changes in lattice parameters *a* and *c* which underlines that our experimentally determined lattice parameters for pristine and B-doped NCM811 are almost identical and do not strongly depend on B-doping.

As shown above, the STEM analysis of the synthesized cathode materials indicated that B-doping of NCM811 affects the surface region of the cathode material. However, the B-doped cathode materials synthesized within this work do not show the expected arrangement of the primary particles within the agglomerates as known for the highly Ni-enriched NCM90.[37] Instead, we saw an influence of B-doping on the lattice parameter, cation disorder, and powder morphology. Since the detection of boron in a single primary particle by electron energy loss spectroscopy (EELS) was not successful, we applied advanced ion beam analysis to experimentally verify the exact location of boron in 2B-NCM811. In order to analyze the NCM811 host structure, Rutherford backscattering (RBS) was used since it is sensitive to heavy elements and has good depth resolution. The RBS part of the spectrum interesting for NCM811 is displayed in **Figure 5**a. It gives information about the composition of the heavy elements Ni, Co and Mn in the NCM811 powder. A comparison between the experimental and simulated data shows that there is a depletion of Ni, Co and Mn on the surface of the secondary particles, leading to a lower experimental signal compared to the simulation which assumes homogenous NCM811 particles. The thickness of the depletion layer is around 400 nm and can be attributed to surface impurities (e.g. carbonates, hydroxides, etc.) or due to the presence of boron on the particle surface. In the core of the particles, a homogenous composition of NCM811 is observed, indicated by a perfect fitting between experimental and simulated values. In contrast to RBS, nuclear reaction analysis (NRA) enables the selective detection of light elements like lithium and boron with a penetration depth of up to 5 µm. The NRA part of the spectrum (**Figure 5**b) shows the boron signal. For this measurement, the shown length scale for the boron detection is around 2 µm with a similar depth resolution. The detected B-NRA signal emphasizes a surface enrichment of boron. The quantification of boron based on NRA shows an average concentration of (3 ± 1) mol% boron in the first 2 µm of the analyzed particles. When considering the measurement uncertainties, the found boron amount by NRA is in good agreement with the expected 2 mol% boron verified by ICP-OES (Table S1). Even though this is not a direct proof that boron is homogenously distributed in the crystal structure, the results indicate that boron is distributed on the secondary particle surface. If boron is also present in the interior of the primary NCM particles needs to be further analyzed.

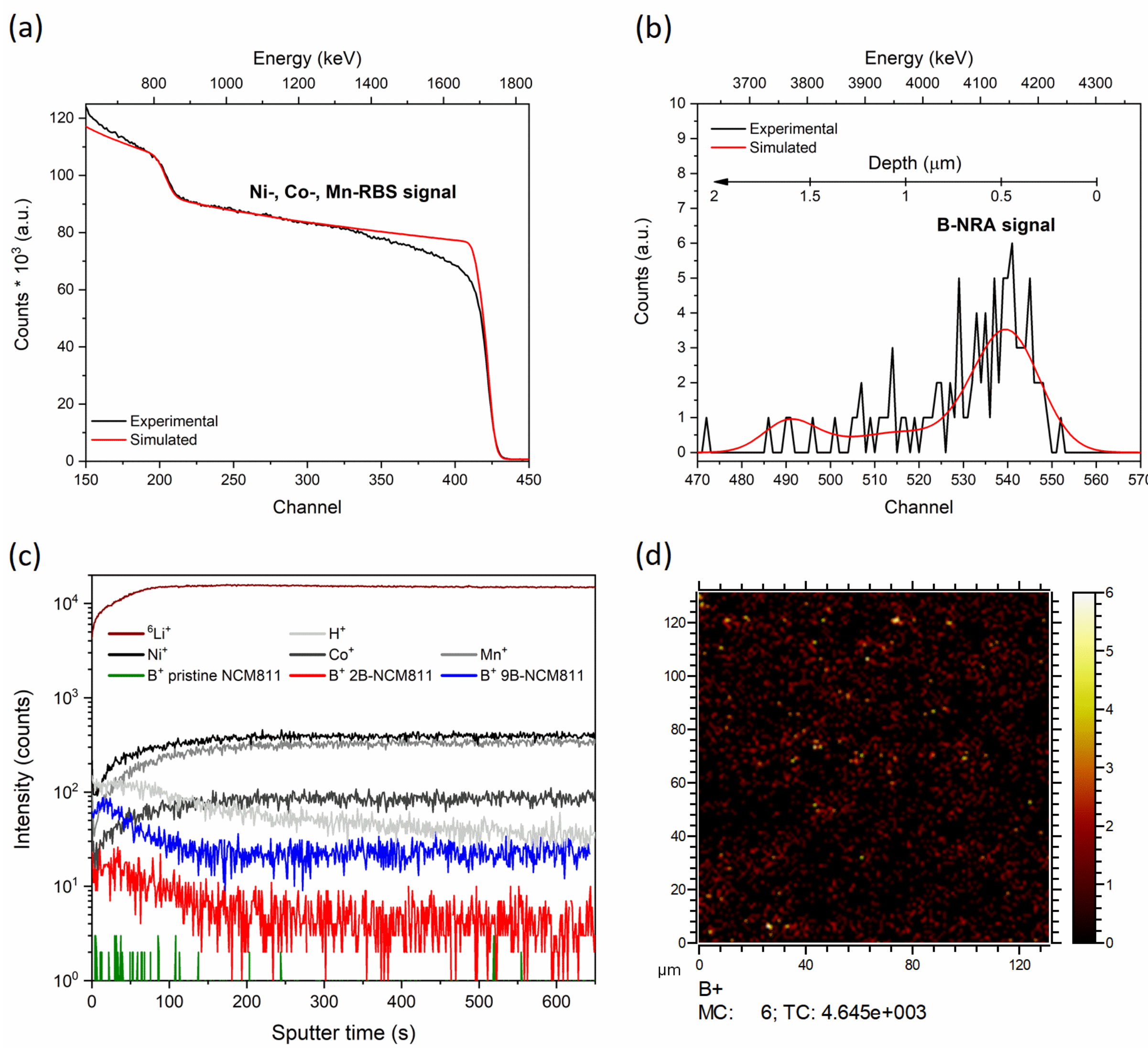

Figure 5. Detection and localization of boron in 2B-NCM811. (a) RBS spectrum showing measured and simulated data. (b) NRA spectrum showing the B-signal. (c) TOF-SIMS depth profiles and (d) boron mapping for 2B-NCM811. In (c), additionally the depth profiles of B^+ for pristine and 9B-NCM811 were shown. For those samples Li^+, H^+ and the transition metal ions are identical and are not shown for simplification.

To address this question, the surface of 2B-NCM811 was characterized by time of flight-secondary ion mass spectrometry (TOF-SIMS) with positive polarity. TOF-SIMS is a technique with ultrahigh chemical selectivity that provides a high sensitivity in detection of different elements like TM cations but also the light cations lithium and boron with depth resolution.[71] The TOF-SIMS depth profiling as well as the mapping of boron for 2B-NCM811 is shown in **Figure 5**c,d. The depth profiles show that the Li^+, Co^+, Ni^+ and Mn^+ signals increase and stay constant after 100 s sputter time, which is in agreement with the RBS observations. Possibly, sputter ions remove surface contaminations (e.g. carbonates, hydroxides, etc.) formed during the transfer of the samples to the instrument, and after a while a fresh layer is reached meaning a constant signal. This suggestion is underlined by the H^+-signal that stays constant during the first 80 s sputtering and continuously decreases afterwards. Furthermore, an enrichment of another element, probably boron, is the reason for the increasing intensity of the Li^+, Co^+, Ni^+ and Mn^+ signals. More importantly, the B^+-signal in all B-doped NCM samples decays with the sputter time and stays constant after 150 s sputtering. The B^+-signal of 2B-NCM811 is close to the detection limit. The samples containing 9 mol% boron (9B-NCM811) and pristine NCM811 were additionally analyzed to confirm that the observed signal really results from boron in NCM811. In case of higher B-concentration (9B-NCM811), the signal intensity observed for 2B-NCM811 was increased by exactly a factor of 4.5. For pristine NCM811 no intensity for B^+ was found, which strongly indicates that the recorded signal corresponds to boron in B-doped NCM811 and linearly increases with the corresponding boron concentration. The boron mapping (**Figure 5**d) demonstrates that boron is homogenously distributed throughout the analyzed particles. Depth profiling via TOF-SIMS confirms a slight concentration gradient of boron from the surface to the bulk where the B-concentration stays constant. The results of TOF-SIMS analysis support the conclusions of XRD, TEM and NRA analyses presented above that the boron is incorporated in the bulk structure of the primary particles core, and additionally boron enriches the agglomerate surface.

To finally investigate the effects of boron incorporation into the NCM lattice and its enrichment on the secondary particle surface on the electrochemical properties of NCM811, electrochemical tests were performed. Here, NCM811 with 2 mol% B-doping was chosen as an optimum composition to study the effects of B-doping on the electrochemical performance since the lower doping levels were already investigated before[37] and the higher doping levels are expected to demonstrate an inferior electrochemical performance due a strongly enhanced degree of cation disorder. The electrochemical characterization of pristine NCM811 and 2B-NCM811 (Figure S5) demonstrates that the materials are electrochemically active but the low discharge capacities of around 160 mAh g^{-1} are not satisfactory for Ni-rich NCM811. These reduced capacities can be attributed to the enhanced cation disorder reported above (**Table 1**). In order to optimize the electrochemical performance, two additional samples (NCM811_o and 2B-NCM811_o) were synthesized under an increased oxygen partial pressure during calcination. Calcination under higher oxygen partial pressure reduces cation disorder and enhances capacities but does not change the basic structure and morphology (Figure S6, Figure S7, Figure S8 and Table S4), so that our fundamental findings about cation disorder, lattice position and localization of boron remain valid.

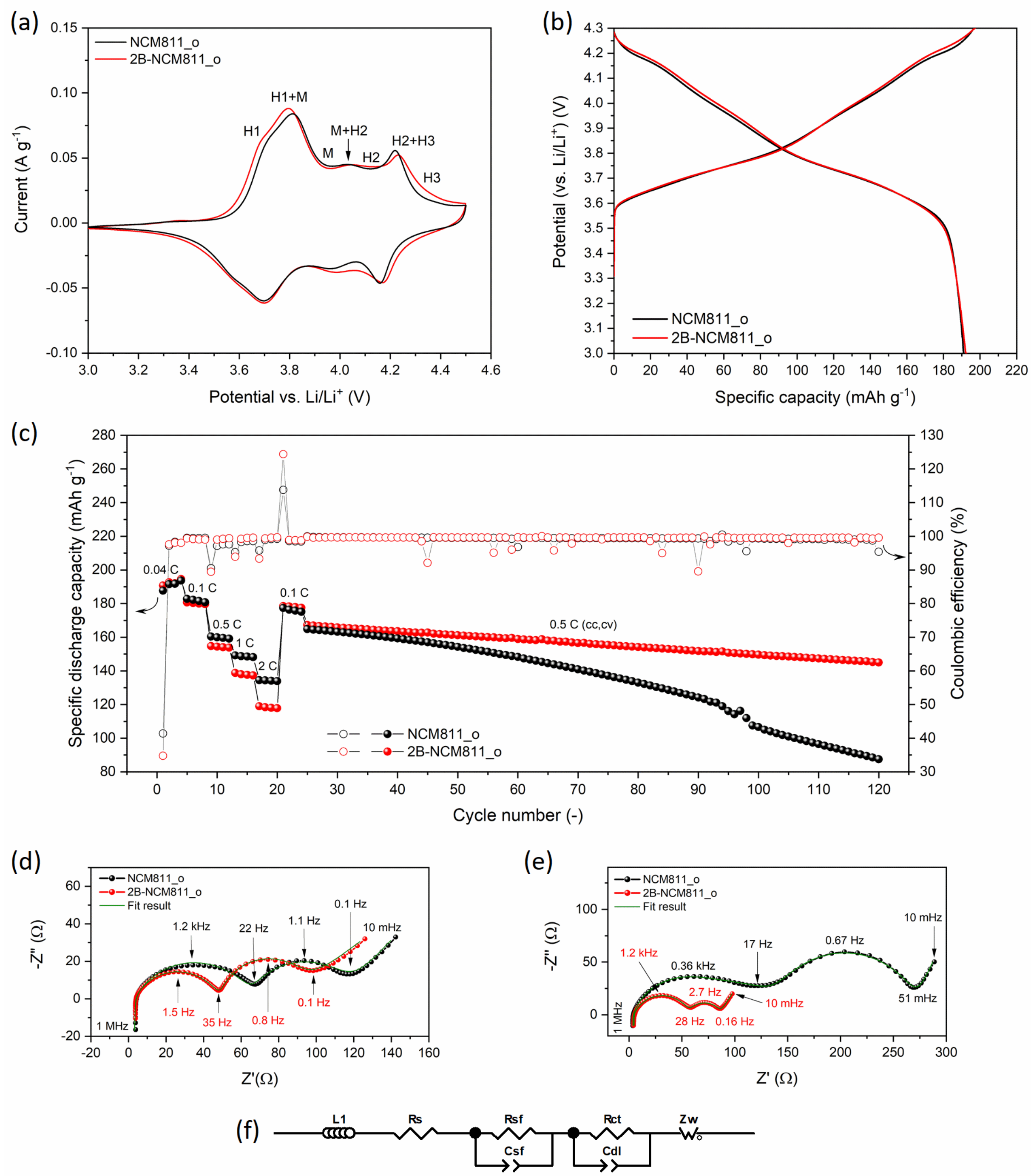

Figure 6. Electrochemical performance of NCM811_o and 2B-NCM811_o. (a) Cyclic voltammograms curves at a scan rate of 0.05 mV s^{-1} for the 2nd cycle, (b) galvanostatic charge-discharge profiles at 0.04 C for the 2nd cycle, (c) rate capability tests at various C-rates with

prolonged cycling at 0.5 C (cc, cv), Electrochemical impedance spectra: (d) Nyquist plot after four cycles at 0.04 C, (e) Nyquist plot after 120 cycles and (f) equivalent circuit model.

Cyclic voltammetry (CV) curves of pristine NCM811_o and 2B-NCM811_o (**Figure 6**a) confirm their electrochemical activity. The shape of the CV curves does not change dramatically by B-doping. Both cathode materials show multiple redox peaks corresponding to phase transitions. During delithiation the original hexagonal structure (H1) transforms into monoclinic (M) and further to other hexagonal structures (H2 and H3). The transition from H2 to H3 is known to cause a detrimental lattice shrinkage in *c*-direction leading to mechanical degradation.[72] The redox peaks for Ni^{2+}/Ni^{4+} are found at 3.81/3.70 V and 3.79/3.70 V for pristine NCM811_o and 2B-NCM811_o, respectively. Additionally, redox peaks were found at 4.22/4.16 V for pristine NCM811_o and at 4.23/4.17 V for 2B-NCM811_o, corresponding to Co^{3+}/Co^{4+}. For 2B-NCM811_o, the potential difference between oxidation and reduction peak for the redox couple at around 3.80 V (0.09 V) is smaller than for pristine NCM811 (0.11 V), indicating a favorable effect of B-doping on the electrochemical activity. The reduced polarization by B-doping is more obvious in the first CV scan (Figure S9). All these findings are consistent with previous studies about B-doped NCM.[37, 38]

Galvanostatic charge/discharge analysis confirms that the incorporation of the electrochemical inactive element boron does not lead to a significantly reduced capacity. After an initial conditioning cycle, discharge capacities of 188 mAh g^{-1} and 191 mAh g^{-1} were obtained for pristine NCM811_o and 2B-NCM811_o, respectively (**Figure 6**b). The coulombic efficiencies are 97 % for NCM811_o and 98 % for 2B-NCM811_o. A distinct impact of B-doping on the electrochemical performance of NCM811 was found during rate capability tests and long-term cycling. While at low C-rates (0.04 C and 0.1 C) similar capacities were obtained for NCM811_o and 2B-NCM811_o, at higher C-rates (0.5 – 2 C) the B-doped NCM shows always lower capacities compared to the undoped active material (**Figure 6**c). The effect of boron on the discharge capacities at high C-rates appears to be more pronounced than previously reported for lower B-concentration in highly Ni-enriched NCM.[37] The lower capacities for 2B-NCM811 under high discharge rates can be explained by a reduced electronic conductivity due to B-doping as previously reported by K.-J. Park *et al.*[37] and the enhanced cation disorder caused by B-doping (**Table 1** and Table S4). However, the positive effect of B-doping is clearly observed during the prolonged cycling at 0.5 C (**Figure 6**c), where 2B-NCM811_o shows significantly reduced capacity fading as compared to pristine NCM811_o. The capacity retention after 120 cycles is 87 % for 2B-NCM811_o and only 53 % for pristine NCM811_o. For both cathodes similar Coulombic efficiencies between 90 – 99 % were obtained during long-term cycling.

Electrochemical impedance spectroscopy (EIS) was applied to study the effect of B-doping on the surface-film and charge-transfer resistance after four (**Figure 6**d) and 120 charge/discharge cycles (**Figure 6**e). The fitting of the data was performed by using the equivalent circuit depicted in **Figure 6**f. In case of pristine NCM811_o the surface-film resistance in the high frequency range increases during cycling from 63 Ω to 105 Ω and the charge-transfer resistance in the low frequency range also increased from 49 Ω after four to 187 Ω after 120 cycles which is in agreement with the strong capacity fading observed for NCM811_o (**Figure 6**c). In case of 2B-NCM811_o, the surface-film and charge-transfer resistance are initially smaller than for pristine NCM811_o and do not strongly change after long-term cycling. The surface-film resistance slightly increases during cycling from 45 Ω to 53 Ω while the charge-transfer resistance decreases from 37 Ω to 28 Ω. The stable surface-film and charge-transfer resistances as well as the improved cycling stability found for 2B-NCM811_o are possible effects of B-doping which positively effects the electrochemical performance of NCM811.

Since an easier stress release due to radial aligned primary particles is not the reason for the here observed improved capacity retention of B-doped NCM811_o during long-term cycling, we assume that the reported B-enrichment on the secondary particle surface acts as a protective surface coating which protects the NCM particles from direct contact with the electrolyte and thus suppresses side reactions at the electrode-electrolyte interface. Such a performance improvement by boron containing coatings was previously reported by S. N. Lim *et al.*[73] and K. Lee *et al.*[74]. In our case the coatings are much thinner and even not visible by TEM. Additionally, the observed thinner, plate-like B-doped NCM811 primary particles possibly profit from more oxygen stable lateral facets as reported by C.-H. Jung *et al.*[43]. This is a possible further explanation for the improved cycling stability without radial aligned primary particles.

4. Conclusion

In this work we have demonstrated the synthesis of B-doped NCM811 via a hydroxide co-precipitation route. Addition of B_2O_3 during the lithiation step leads to a successful incorporation of boron into the NCM lattice. The determined lattice parameters based on X-ray diffraction were not strongly influenced by B-doping, but an increased cation disorder was found with the increasing boron content. Our theoretical study showed that a lattice expansion is suppressed by the increased cation disorder. Furthermore, our theoretical results provide a deep insight into the location of B-atoms in the NCM811 lattice. The simulated lattice structures show that, depending on its doping level, the boron occupies tetrahedral sites in the Ni-layers (2B-NCM811) or both trigonal planar sites in the O-layers and tetrahedral sites in the Ni-layers (4B-NCM811) of the NCM811 lattice. Morphology characterization by SEM showed that the synthesized powders consist of sphere like secondary particles, which are composed of nano-sized primary particles. The incorporation of boron leads to a change in primary particle size and shape which results in a denser surface of the agglomerates and a reduced specific BET surface area. In contrast to the previous reports, the 2B-NCM811 secondary particles did not demonstrate the expected alignment of the primary particles along the radial direction, suggesting that not only B-doping but rather a fine tuning of the synthesis conditions including the pH-value and the ammonia concentration are required to achieve the significant change in particles morphology. Up to now, the precise location of boron in NCM as well as the experimental prove of its incorporation was not reported at all. Therefore, the synthesized 2B-NCM811 material was used as model compound to experimentally detect, quantify, and localize boron by ion beam analysis (NRA) and TOF-SIMS. As a result of this work, we demonstrated that boron is not only located on the surface of the agglomerates but also incorporates into the bulk of the primary particles. We found a slight boron enrichment on the agglomerate surface but also a significant high and constant boron concentration in the bulk of the primary particles. Our findings thus show that the boron localization both in the bulk and at the surface leads to two different effects on the atomic and microstructural scale. In the bulk, the incorporation of boron does not lead to a significant lattice expansion but shows a detrimental effect on the electrochemical performance at high C-rates and increases the cation disorder. In contrast to this, the boron located on the agglomerate surface leads to a decrease in cation disorder, avoids phase transition to rock-salt structure and thus might have beneficial effects on the surface properties, resulting in significantly improved capacity retention during long-term cycling of B-doped NCM811.

ASSOCIATED CONTENT

Supporting Information

The supporting Information is available free of charge. Representation of the chemical analysis by ICP-OES; particle size distributions (PSD) of pristine and 2B-NCM811; values for primary particle size, BET surface area and density of pristine and B-doped NCM811; EDS spectrum and elemental mapping of primary particle and results of Rietveld refinement with cation occupation and structural parameters.

AUTHOR INFORMATION

Corresponding Author

*Martin Finsterbusch: Institute of Energy and Climate Research – Materials Synthesis and Processing, Forschungszentrum Jülich GmbH, Wilhelm Johnen Str., 52425, Jülich, Germany.
E-mail: m.finsterbusch@fz-juelich.de

Author Contributions

C.R. synthesized the samples, performed the electrochemical characterization, analyzed all data and wrote the manuscript with contributions from all authors. L.-Y.K. and P.K. performed the theoretical studies. Y.-J.S. conducted the Rietveld refinements. S.M. performed the ion beam analysis. D.S. took the SEM images. H.V., M.M. and J.M. did the TEM investigations. U.B. conducted the TOF-SIMS. M.F., P.K., O.G. and D.F.-R. initiated the idea, provided the resources and supervised the work. All authors have given approval to the final version of the manuscript.

Notes

The authors declare no competing financial interest.

ACKNOWLEDGMENT

The financial support of this work by the German Federal Ministry of Education and Research (Bundesministerium für Bildung und Forschung, BMBF), under Grant No. 3EK3054A (SimCaMat) and 03XP0258C (MeetHiEnD) is hereby gratefully acknowledged. The authors acknowledge the contributions of Dr. Volker Nischwitz (Central Institute for Engineering, Electronics and Analytics (ZEA-3), Forschungszentrum Jülich GmbH) (ICP-OES), Andrea Hilgers (PSD), Sigrid Schwartz-Lückge (BET surface area and density), Markus Mann (Rietveld refinements) and Volker Bader (heat treatments). P. K. gratefully acknowledges the computing time granted through JARA-HPC on the supercomputer JURECA at Forschungszentrum Jülich.

ABBREVIATIONS

NCM, $Li[Ni_xCo_yMn_z]O_2$; LNO, $LiNiO_2$; LIBs, lithium-ion batteries; CAMs, cathode active materials; EVs, electrical vehicles; TM, transition metal; ICP-OES, inductively coupled plasma-optical emission spectrometry; PSD, particle size distribution; DFT, density functional theory; HAADF-STEM, high-angle annular dark filed scanning transmission electron microscopy; FIB, focused ion beam; EDS, energy dispersive X-ray; EELS, electron energy loss spectroscopy; RBS, Rutherford backscattering; NRA, nuclear reaction analysis; TOF-SIMS, time of flight-secondary ion mass spectrometry; EIS, electrochemical impedance spectroscopy

REFERENCES

(1) Noh, H.-J.; Youn, S.; Yoon, C. S.; Sun, Y.-K., Comparison of the structural and electrochemical properties of layered $Li[Ni_xCo_yMn_z]O_2$ (x = 1/3, 0.5, 0.6, 0.7, 0.8 and 0.85) cathode material for lithium-ion batteries. *Journal of Power Sources* **2013,** 233, 121-130.

(2) Weigel, T.; Schipper, F.; Erickson, E. M.; Susai, F. A.; Markovsky, B.; Aurbach, D., Structural and Electrochemical Aspects of $LiNi_{0.8}Co_{0.1}Mn_{0.1}O_2$ Cathode Materials Doped by Various Cations. *ACS Energy Letters* **2019,** 4, (2), 508-516.

(3) Han, S.-H.; Song, J. H.; Yim, T.; Kim, Y.-J.; Yu, J.-S.; Yoon, S., Communication—Improvement of Structural Stability during High-Voltage Cycling in High-Nickel Cathode Materials with B_2O_3Addition. *Journal of The Electrochemical Society* **2016,** 163, (5), A748-A750.

(4) Kim, U.-H.; Park, G.-T.; Son, B.-K.; Nam, G. W.; Liu, J.; Kuo, L.-Y.; Kaghazchi, P.; Yoon, C. S.; Sun, Y.-K., Heuristic solution for achieving long-term cycle stability for Ni-rich layered cathodes at full depth of discharge. *Nature Energy* **2020,** 5, (11), 860-869.

(5) Eilers-Rethwisch, M.; Winter, M.; Schappacher, F. M., Synthesis, electrochemical investigation and structural analysis of doped $Li[Ni_{0.6}Mn_{0.2}Co_{0.2-x}M_x]O_2$ (x = 0, 0.05; M = Al, Fe, Sn) cathode materials. *Journal of Power Sources* **2018,** 387, 101-107.

(6) Yan, W.; Yang, S.; Huang, Y.; Yang, Y.; Guohui, Y., A review on doping/coating of nickel-rich cathode materials for lithium-ion batteries. *Journal of Alloys and Compounds* **2020,** 819, 153048.

(7) Sun, Y.-K.; Myung, S.-T.; Park, B.-C.; Prakash, J.; Belharouak, I.; Amine, K., High-energy cathode material for long-life and safe lithium batteries. *Nature Materials* **2009,** 8, 320.

(8) Liao, J.-Y.; Manthiram, A., Surface-modified concentration-gradient Ni-rich layered oxide cathodes for high-energy lithium-ion batteries. *Journal of Power Sources* **2015,** 282, 429-436.

(9) Liang, L.; Du, K.; Lu, W.; Peng, Z.; Cao, Y.; Hu, G., Synthesis and characterization of concentration–gradient $LiNi_{0.6}Co_{0.2}Mn_{0.2}O_2$ cathode material for lithium ion batteries. *Journal of Alloys and Compounds* **2014,** 613, 296-305.

(10) Kim, U.-H.; Ryu, H.-H.; Kim, J.-H.; Mücke, R.; Kaghazchi, P.; Yoon, C. S.; Sun, Y.-K., Microstructure-Controlled Ni-Rich Cathode Material by Microscale Compositional Partition for Next-Generation Electric Vehicles. *Advanced Energy Materials* **2019,** 9, (15), 1803902.

(11) Hou, P.; Wang, X.; Wang, D.; Song, D.; Shi, X.; Zhang, L.; Guo, J.; Zhang, J., A novel core-concentration gradient-shelled $LiNi_{0.5}Co_{0.2}Mn_{0.3}O_2$ as high-performance cathode for lithium-ion batteries. *RSC Advances* **2014,** 4, (31), 15923-15929.

(12) Dou, J.; Kang, X.; Wumaier, T.; Yu, H.; Hua, N.; Han, Y.; Xu, G., Effect of lithium boron oxide glass coating on the electrochemical performance of $LiNi_{1/3}Co_{1/3}Mn_{1/3}O_2$. *Journal of Solid State Electrochemistry* **2012,** 16, (4), 1481-1486.

(13) Li, X.; Jin, L.; Song, D.; Zhang, H.; Shi, X.; Wang, Z.; Zhang, L.; Zhu, L., $LiNbO_3$-coated $LiNi_{0.8}Co_{0.1}Mn_{0.1}O_2$ cathode with high discharge capacity and rate performance for all-solid-state lithium battery. *Journal of Energy Chemistry* **2020,** 40, 39-45.

(14) Zhang, J.; Li, Z.; Gao, R.; Hu, Z.; Liu, X., High Rate Capability and Excellent Thermal Stability of Li^+-Conductive Li_2ZrO_3-Coated $LiNi_{1/3}Co_{1/3}Mn_{1/3}O_2$ via a Synchronous Lithiation Strategy. *The Journal of Physical Chemistry C* **2015,** 119, (35), 20350-20356.

(15) Bai, X.; Li, W.; Zhang, L.; Liu, Z. In *Effects of $LiAlO_2$ coating on electrochemical performance of single-crystal $LiNi_{0.6}Co_{0.2}Mn_{0.2}O_2$*, IOP Conference Series: Earth and Environmental Science, 2018; IOP Publishing: 2018; p 032050.

(16) Okada, K.; Machida, N.; Naito, M.; Shigematsu, T.; Ito, S.; Fujiki, S.; Nakano, M.; Aihara, Y., Preparation and electrochemical properties of $LiAlO_2$-coated $Li(Ni_{1/3}Mn_{1/3}Co_{1/3})O_2$ for all-solid-state batteries. *Solid State Ionics* **2014,** 255, 120-127.

(17) Wu, J.; Tan, X.; Zhang, J.; Guo, L.; Jiang, Y.; Liu, S.; Zhao, T.; Liu, Y.; Ren, J.; Wang, H.; Kang, X.; Chu, W., Improvement of Electrochemical Performance of Nickel Rich $LiNi_{0.8}Co_{0.1}Mn_{0.1}O_2$ Cathode by Lithium Aluminates Surface Modifications. *Energy Technology* **2019,** 7, (2), 209-215.

(18) Zhang, X.-D.; Shi, J.-L.; Liang, J.-Y.; Wang, L.-P.; Yin, Y.-X.; Jiang, K.-C.; Guo, Y.-G., An effective $LiBO_2$ coating to ameliorate the cathode/electrolyte interfacial issues of $LiNi_{0.6}Co_{0.2}Mn_{0.2}O_2$ in solid-state Li batteries. *Journal of Power Sources* **2019,** 426, 242-249.

(19) You, L.; Chu, B.; Li, G.; Huang, T.; Yu, A., H_3BO_3 washed $LiNi_{0.8}Co_{0.1}Mn_{0.1}O_2$ with enhanced electrochemical performance and storage characteristics. *Journal of Power Sources* **2021,** 482, 228940.

(20) Sun, Y.-K.; Myung, S.-T.; Kim, M.-H.; Prakash, J.; Amine, K., Synthesis and Characterization of $Li[(Ni_{0.8}Co_{0.1}Mn_{0.1})_{0.8}(Ni_{0.5}Mn_{0.5})_{0.2}]O_2$ with the Microscale Core−Shell Structure as the Positive Electrode Material for Lithium Batteries. *Journal of the American Chemical Society* **2005,** 127, (38), 13411-13418.

(21) Hou, P.; Zhang, H.; Zi, Z.; Zhang, L.; Xu, X., Core–shell and concentration-gradient cathodes prepared via co-precipitation reaction for advanced lithium-ion batteries. *Journal of Materials Chemistry A* **2017,** 5, (9), 4254-4279.

(22) Lee, K.-S.; Myung, S.-T.; Sun, Y.-K., Synthesis and electrochemical performances of core-shell structured $Li[(Ni_{1/3}Co_{1/3}Mn_{1/3})_{0.8}(Ni_{1/2}Mn_{1/2})_{0.2}]O_2$ cathode material for lithium ion batteries. *Journal of Power Sources* **2010,** 195, (18), 6043-6048.

(23) Shi, H.; Wang, X.; Hou, P.; Zhou, E.; Guo, J.; Zhang, J.; Wang, D.; Guo, F.; Song, D.; Shi, X.; Zhang, L., Core–shell structured $Li[(Ni_{0.8}Co_{0.1}Mn_{0.1})_{0.7}(Ni_{0.45}Co_{0.1}Mn_{0.45})_{0.3}]O_2$ cathode material for high-energy lithium ion batteries. *Journal of Alloys and Compounds* **2014,** 587, 710-716.

(24) Hou, P.; Wang, X.; Song, D.; Shi, X.; Zhang, L.; Guo, J.; Zhang, J., Design, synthesis, and performances of double-shelled $LiNi_{0.5}Co_{0.2}Mn_{0.3}O_2$ as cathode for long-life and safe Li-ion battery. *Journal of Power Sources* **2014,** 265, 174-181.

(25) Song, D.; Hou, P.; Wang, X.; Shi, X.; Zhang, L., Understanding the Origin of Enhanced Performances in Core–Shell and Concentration-Gradient Layered Oxide Cathode Materials. *ACS Applied Materials & Interfaces* **2015,** 7, (23), 12864-12872.

(26) Mu, L.; Lin, R.; Xu, R.; Han, L.; Xia, S.; Sokaras, D.; Steiner, J. D.; Weng, T.-C.; Nordlund, D.; Doeff, M. M.; Liu, Y.; Zhao, K.; Xin, H. L.; Lin, F., Oxygen Release Induced Chemomechanical Breakdown of Layered Cathode Materials. *Nano Letters* **2018,** 18, (5), 3241-3249.

(27) Luo, W.; Zhou, F.; Zhao, X.; Lu, Z.; Li, X.; Dahn, J. R., Synthesis, Characterization, and Thermal Stability of $LiNi_{1/3}Mn_{1/3}Co_{1/3-z}Mg_zO_2$, $LiNi_{1/3-z}Mn_{1/3}Co_{1/3}Mg_zO_2$, and $LiNi_{1/3}Mn_{1/3-z}Co_{1/3}Mg_zO_2$. *Chemistry of Materials* **2010,** 22, (3), 1164-1172.

(28) Samarasingha, P. B.; Wijayasinghe, A.; Behm, M.; Dissanayake, L.; Lindbergh, G., Development of cathode materials for lithium ion rechargeable batteries based on the system $Li(Ni_{1/3}Mn_{1/3}Co_{(1/3-x)}M_x)O_2$, (M=Mg, Fe, Al and x=0.00 to 0.33). *Solid State Ionics* **2014,** 268, 226-230.

(29) Nayak, P. K.; Grinblat, J.; Levi, M.; Levi, E.; Kim, S.; Choi, J. W.; Aurbach, D., Al Doping for Mitigating the Capacity Fading and Voltage Decay of Layered Li and Mn-Rich Cathodes for Li-Ion Batteries. *Advanced Energy Materials* **2016,** 6, (8), 1502398.

(30) Kim, U.-H.; Myung, S.-T.; Yoon, C. S.; Sun, Y.-K., Extending the Battery Life Using an Al-Doped Li [$Ni_{0.76}Co_{0.09}Mn_{0.15}$] O_2 Cathode with Concentration Gradients for Lithium Ion Batteries. *ACS Energy Letters* **2017,** 2, (8), 1848-1854.

(31) Zhou, F.; Zhao, X.; Lu, Z.; Jiang, J.; Dahn, J. R., The effect of Al substitution on the reactivity of delithiated $LiNi_{1/3}Mn_{1/3}Co_{(1/3-z)}Al_zO_2$ with non-aqueous electrolyte. *Electrochemistry Communications* **2008,** 10, (8), 1168-1171.

(32) Wang, M.; Chen, Y.; Zhang, L.; Chen, L. In *The doping effect on the electrochemical performance of* $LiNi_{0.305}Mn_{0.33}Co_{0.33}M_{0.025}O_2$ *(M=Al, Y, Cr) for lithium-ion batteries*, 2013 International Conference on Materials for Renewable Energy and Environment, 19-21 Aug. 2014, 2013; 2013; pp 532-536.

(33) Kam, K. C.; Mehta, A.; Heron, J. T.; Doeff, M. M., Electrochemical and Physical Properties of Ti-Substituted Layered Nickel Manganese Cobalt Oxide (NMC) Cathode Materials. *Journal of The Electrochemical Society* **2012,** 159, (8), A1383-A1392.

(34) Jia, X.; Yan, M.; Zhou, Z.; Chen, X.; Yao, C.; Li, D.; Chen, D.; Chen, Y., Nd-doped $LiNi_{0.5}Co_{0.2}Mn_{0.3}O_2$ as a cathode material for better rate capability in high voltage cycling of Li-ion batteries. *Electrochimica Acta* **2017,** 254, 50-58.

(35) Yu, A.; Subba Rao, G. V.; Chowdari, B. V. R., Synthesis and properties of $LiGa_xMg_yNi_{1-x-y}O_2$ as cathode material for lithium ion batteries. *Solid State Ionics* **2000,** 135, (1), 131-135.

(36) Schipper, F.; Dixit, M.; Kovacheva, D.; Talianker, M.; Haik, O.; Grinblat, J.; Erickson, E. M.; Ghanty, C.; Major, D. T.; Markovsky, B., Stabilizing nickel-rich layered cathode materials by a high-charge cation doping strategy: zirconium-doped $LiNi_{0.6}Co_{0.2}Mn_{0.2}O_2$. *Journal of Materials Chemistry A* **2016,** 4, (41), 16073-16084.

(37) Park, K.-J.; Jung, H.-G.; Kuo, L.-Y.; Kaghazchi, P.; Yoon, C. S.; Sun, Y.-K., Improved Cycling Stability of $Li[Ni_{0.90}Co_{0.05}Mn_{0.05}]O_2$ Through Microstructure Modification by Boron Doping for Li-Ion Batteries. *Advanced Energy Materials* **2018,** 8, (25), 1801202.

(38) Lee, S.-H.; Jin, B.-S.; Kim, H.-S., Superior Performances of B-doped $LiNi_{0.84}Co_{0.10}Mn_{0.06}O_2$ cathode for advanced LIBs. *Scientific Reports* **2019,** 9, (1), 17541.

(39) Susai, F. A.; Kovacheva, D.; Chakraborty, A.; Kravchuk, T.; Ravikumar, R.; Talianker, M.; Grinblat, J.; Burstein, L.; Kauffmann, Y.; Major, D. T.; Markovsky, B.; Aurbach, D., Improving Performance of $LiNi_{0.8}Co_{0.1}Mn_{0.1}O_2$ Cathode Materials for Lithium-Ion Batteries by Doping with Molybdenum-Ions: Theoretical and Experimental Studies. *ACS Applied Energy Materials* **2019,** 2, (6), 4521-4534.

(40) Kim, U.-H.; Jun, D.-W.; Park, K.-J.; Zhang, Q.; Kaghazchi, P.; Aurbach, D.; Major, D.; Goobes, G.; Dixit, M.; Leifer, N., Pushing the limit of layered transition metal oxide cathodes for high-energy density rechargeable Li ion batteries. *Energy & Environmental Science* **2018,** 11, (5), 1271-1279.

(41) Park, G.-T.; Ryu, H.-H.; Park, N.-Y.; Yoon, C. S.; Sun, Y.-K., Tungsten doping for stabilization of $Li[Ni_{0.90}Co_{0.05}Mn_{0.05}]O_2$ cathode for Li-ion battery at high voltage. *Journal of Power Sources* **2019,** 442, 227242.

(42) Pan, L.; Xia, Y.; Qiu, B.; Zhao, H.; Guo, H.; Jia, K.; Gu, Q.; Liu, Z., Structure and electrochemistry of B doped $Li(Li_{0.2}Ni_{0.13}Co_{0.13}Mn_{0.54})_{1-x}B_xO_2$ as cathode materials for lithium-ion batteries. *Journal of Power Sources* **2016,** 327, 273-280.

(43) Jung, C.-H.; Kim, D.-H.; Eum, D.; Kim, K.-H.; Choi, J.; Lee, J.; Kim, H.-H.; Kang, K.; Hong, S.-H., New Insight into Microstructure Engineering of Ni-Rich Layered Oxide Cathode for High Performance Lithium Ion Batteries. *Advanced Functional Materials* **2021,** 31, (18), 2010095.

(44) Lee, M. H.; Kang, Y. J.; Myung, S. T.; Sun, Y. K., Synthetic optimization of $Li[Ni_{1/3}Co_{1/3}Mn_{1/3}]O_2$ via co-precipitation. *Electrochimica Acta* **2004,** 50, (4), 939-948.

(45) Shizuka, K.; Okahara, K., Layered lithium nickel manganese cobalt composite oxide powder for material of positive electrode of lithium secondary battery, process for producing the same, positive electrode of lithium secondary battery therefrom, and lithium secondary battery. In Google Patents: 2013.

(46) Degen, T.; Sadki, M.; Bron, E.; König, U.; Nénert, G., The HighScore suite. *Powder Diffraction* **2014,** 29, (S2), S13-S18.

(47) Bruker *AXS, Topas V4: General profile and structure analysis software for powder diffraction data*, Karlsruhe, Germany.

(48) Rodríguez-Carvajal, J., Recent advances in magnetic structure determination by neutron powder diffraction. *Physica B: Condensed Matter* **1993,** 192, (1), 55-69.

(49) Kovács, A.; Schierholz, R.; Tillmann, K., FEI Titan G2 80-200 CREWLEY. *Journal of large-scale research facilities JLSRF* **2016,** 2, 43.

(50) Möller, S.; Höschen, D.; Kurth, S.; Esser, G.; Hiller, A.; Scholtysik, C.; Dellen, C.; Linsmeier, C., A New High-Throughput Focused MeV Ion-Beam Analysis Setup. *Instruments* **2021,** 5, (1), 10.

(51) Chen, H.; Wang, X. M.; Shao, L.; Liu, J. R.; Yen, A. C.; Chu, W.-k., Cross-sections of $^{10}B(\alpha, p)^{13}C$ nuclear reaction for boron analysis. *Nuclear Instruments and Methods in Physics Research Section B: Beam Interactions with Materials and Atoms* **2003,** 211, (1), 1-6.

(52) Mayer, M., *SIMNRA user's guide*. Max-Planck-Institut für Plasmaphysik Garching: 1997.

(53) Blöchl, P. E., Projector augmented-wave method. *Physical review B* **1994,** 50, (24), 17953.

(54) Kresse, G.; Furthmüller, J., Efficient iterative schemes for ab initio total-energy calculations using a plane-wave basis set. *Physical Review B* **1996,** 54, (16), 11169-11186.

(55) Perdew, J. P.; Burke, K.; Ernzerhof, M., Generalized gradient approximation made simple. *Physical review letters* **1996,** 77, (18), 3865.

(56) Sun, J.; Ruzsinszky, A.; Perdew, J. P., Strongly Constrained and Appropriately Normed Semilocal Density Functional. *Physical Review Letters* **2015,** 115, (3), 036402.

(57) Okhotnikov, K.; Charpentier, T.; Cadars, S., Supercell program: a combinatorial structure-generation approach for the local-level modeling of atomic substitutions and partial occupancies in crystals. *Journal of cheminformatics* **2016,** 8, (1), 1-15.

(58) Kuo, L.-Y.; Guillon, O.; Kaghazchi, P., Origin of Structural Phase Transitions in Ni-Rich $Li_xNi_{0.8}Co_{0.1}Mn_{0.1}O_2$ with Lithiation/Delithiation: A First-Principles Study. *ACS Sustainable Chemistry & Engineering* **2021,** 9, (22), 7437-7446.

(59) Chang, C.-C.; Kumta, P. N., Mechanochemical synthesis of $LiNiO_2$. *Materials Science and Engineering: B* **2005,** 116, (3), 341-345.

(60) Zhu, J.; Vo, T.; Li, D.; Lu, R.; Kinsinger, N. M.; Xiong, L.; Yan, Y.; Kisailus, D., Crystal Growth of $Li[Ni_{1/3}Co_{1/3}Mn_{1/3}]O_2$ as a Cathode Material for High-Performance Lithium Ion Batteries. *Crystal Growth & Design* **2012,** 12, (3), 1118-1123.

(61) Du, B.; Mo, Y.; Jin, H.; Li, X.; Qu, Y.; Li, D.; Cao, B.; Jia, X.; Lu, Y.; Chen, Y., Radially Microstructural Design of $LiNi_{0.8}Co_{0.1}Mn_{0.1}O_2$ Cathode Material toward Long-Term Cyclability and High Rate Capability at High Voltage. *ACS Applied Energy Materials* **2020,** 3, (7), 6657-6669.

(62) Kramer, D.; Ceder, G., Tailoring the Morphology of $LiCoO_2$: A First Principles Study. *Chemistry of Materials* **2009,** 21, (16), 3799-3809.

(63) Kondrakov, A. O.; Geßwein, H.; Galdina, K.; de Biasi, L.; Meded, V.; Filatova, E. O.; Schumacher, G.; Wenzel, W.; Hartmann, P.; Brezesinski, T.; Janek, J., Charge-Transfer-Induced Lattice Collapse in Ni-Rich NCM Cathode Materials during Delithiation. *The Journal of Physical Chemistry C* **2017,** 121, (44), 24381-24388.

(64) Friedrich, F.; Strehle, B.; Freiberg, A. T. S.; Kleiner, K.; Day, S. J.; Erk, C.; Piana, M.; Gasteiger, H. A., Editors' Choice—Capacity Fading Mechanisms of NCM-811 Cathodes in Lithium-Ion Batteries Studied by X-ray Diffraction and Other Diagnostics. *Journal of The Electrochemical Society* **2019,** 166, (15), A3760-A3774.

(65) Zheng, X.; Li, X.; Zhang, B.; Wang, Z.; Guo, H.; Huang, Z.; Yan, G.; Wang, D.; Xu, Y., Enhanced electrochemical performance of $LiNi_{0.8}Co_{0.1}Mn_{0.1}O_2$ cathode materials obtained by atomization co-precipitation method. *Ceramics International* **2016,** 42, (1, Part A), 644-649.

(66) Gao, S.; Cheng, Y.-T.; Shirpour, M., Effects of Cobalt Deficiency on Nickel-Rich Layered $LiNi_{0.8}Co_{0.1}Mn_{0.1}O_2$ Positive Electrode Materials for Lithium-Ion Batteries. *ACS Applied Materials & Interfaces* **2019,** 11, (1), 982-989.

(67) Hua, W.; Schwarz, B.; Knapp, M.; Senyshyn, A.; Missiul, A.; Mu, X.; Wang, S.; Kübel, C.; Binder, J. R.; Indris, S.; Ehrenberg, H., (De) Lithiation Mechanism of Hierarchically Layered $LiNi_{1/3}Co_{1/3}Mn_{1/3}O_2$ Cathodes during High-Voltage Cycling. *Journal of The Electrochemical Society* **2018,** 166, (3), A5025.

(68) Choi, Y.-M.; Pyun, S.-I.; Moon, S.-I., Effects of cation mixing on the electrochemical lithium intercalation reaction into porous $Li_{1-\delta}Ni_{1-y}Co_yO_2$ electrodes. *Solid State Ionics* **1996,** 89, (1), 43-52.

(69) Gurr, G.; Montgomery, P.; Knutson, C.; Gorres, B., The crystal structure of trigonal diboron trioxide. *Acta Crystallographica Section B: Structural Crystallography and Crystal Chemistry* **1970,** 26, (7), 906-915.

(70) Prewitt, C.; Shannon, R., Crystal structure of a high-pressure form of B_2O_3. *Acta Crystallographica Section B: Structural Crystallography and Crystal Chemistry* **1968,** 24, (6), 869-874.

(71) Xie, Q.; Li, W.; Dolocan, A.; Manthiram, A., Insights into Boron-based Polyanion-tuned High-nickel Cathodes for High-energy-density Lithium-ion Batteries. *Chemistry of Materials* **2019,** 31, (21), 8886-8897.

(72) Ryu, H.-H.; Park, K.-J.; Yoon, C. S.; Sun, Y.-K., Capacity Fading of Ni-Rich $Li[Ni_xCo_yMn_{1-x-y}]O_2$ ($0.6 \leq x \leq 0.95$) Cathodes for High-Energy-Density Lithium-Ion Batteries: Bulk or Surface Degradation? *Chemistry of Materials* **2018,** 30, (3), 1155-1163.

(73) Lim, S. N.; Ahn, W.; Yeon, S.-H.; Park, S. B., Enhanced elevated-temperature performance of $Li(Ni_{0.8}Co_{0.15}Al_{0.05})O_2$ electrodes coated with Li_2O-$2B_2O_3$ glass. *Electrochimica Acta* **2014,** 136, 1-9.

(74) Lee, K.; Yang, G. J.; Kim, H.; Kim, T.; Lee, S. S.; Choi, S.-Y.; Choi, S.; Kim, Y., Composite coating of Li_2O–$2B_2O_3$ and carbon as multi-conductive electron/Li-ion channel on the surface of $LiNi_{0.5}Mn_{1.5}O_4$ cathode. *Journal of Power Sources* **2017,** 365, 249-256.

Abstract graphic